

## Article

# Epoxy Resin-Reinforced F-Assisted $\text{Na}_3\text{Zr}_2\text{Si}_2\text{PO}_{12}$ Solid Electrolyte for Solid-State Sodium Metal Batteries

Yao Fu, Dangling Liu, Yongjiang Sun, Genfu Zhao and Hong Guo \*

International Joint Research Center for Advanced Energy Materials of Yunnan Province, Yunnan Key Laboratory of Carbon Neutrality and Green Low-Carbon Technologies, School of Materials and Energy, Yunnan University, Kunming 650091, China

\* Correspondence: guohong@ynu.edu.cn

**Abstract:** Solid sodium ion batteries (SIBs) show a significant amount of potential for development as energy storage systems; therefore, there is an urgent need to explore an efficient solid electrolyte for SIBs.  $\text{Na}_3\text{Zr}_2\text{Si}_2\text{PO}_{12}$  (NZSP) is regarded as one of the most potential solid-state electrolytes (SSE) for SIBs, with good thermal stability and mechanical properties. However, NZSP has low room temperature ionic conductivity and large interfacial impedance. F<sup>-</sup>-doped NZSP has a larger grain size and density, which is beneficial for acquiring higher ionic conductivity, and the composite system prepared with epoxy can further improve density and inhibit Na dendrite growth. The composite system exhibits an outstanding  $\text{Na}^+$  conductivity of  $0.67 \text{ mS cm}^{-1}$  at room temperature and an ionic mobility number of 0.79. It also has a wider electrochemical stability window and cycling stability.

**Keywords:** sodium ion battery; epoxy-NZSPF<sub>0.7</sub>; composite solid electrolyte; solid-state electrolyte



**Citation:** Fu, Y.; Liu, D.; Sun, Y.; Zhao, G.; Guo, H. Epoxy Resin-Reinforced F-Assisted  $\text{Na}_3\text{Zr}_2\text{Si}_2\text{PO}_{12}$  Solid Electrolyte for Solid-State Sodium Metal Batteries. *Batteries* **2023**, *9*, 331. <https://doi.org/10.3390/batteries9060331>

Academic Editors: Chunwen Sun, Siqi Shi, Yongjie Zhao, Yong-Joon Park and Johan E. ten Elshof

Received: 11 April 2023

Revised: 5 June 2023

Accepted: 12 June 2023

Published: 19 June 2023



**Copyright:** © 2023 by the authors. Licensee MDPI, Basel, Switzerland. This article is an open access article distributed under the terms and conditions of the Creative Commons Attribution (CC BY) license (<https://creativecommons.org/licenses/by/4.0/>).

## 1. Introduction

Energy storage systems (ESSs) are gradually becoming essential and important in people's daily lives, as these can provide us with convenience in many aspects [1–4]. As a hopeful substitute for lithium-ion batteries (LIBs), SIBs have caught the attention of a number of researchers recently because of their rich sodium resources, low prices and excellent sustainability. However, because sodium is more reactive than lithium, it is more likely to form dendrites in the conventional liquid electrolyte battery system, posing serious efficiency problems and safety hazards. Hence, research on solid or quasi-solid sodium ion batteries is of great importance for improving battery efficiency and safety [5–16].

To date, different types of sodium materials, such as  $\text{Na}-\beta''-\text{Al}_2\text{O}_3$ , sulfides, polymers, and Na superionic conductor (NASICON) have been reported for use as sodium ion solid-state electrolytes. As a solid electrolyte,  $\text{Na}-\beta''-\text{Al}_2\text{O}_3$  is now successfully used in Na-S batteries; however, it is sensitive to moisture [17] and has a high preparation temperature, which poses some limitations to its production applications. Most sulfide-based solid electrolytes are limited in their application due to their instability in air [18] and narrow electrochemical stability window [19], despite their high ionic conductivity and good ductility. The polymer solid electrolyte is flexible, and the contact between it and the electrode is flexible, which makes it malleable and easy to process and shape. However, the ionic conductivity and ion transfer number dose not meet the imposed requirements when using at room temperature. To achieve ionic conductivity for battery applications, a temperature of  $60^\circ\text{C}$  or higher is required. This temperature approaches the melting point of anode, Na ( $97^\circ\text{C}$ ), which can cause safety problems. By comparing with the sodium-ion solid electrolyte above, a significant amount of attention has been devoted to NASICON ( $\text{Na}_{1+x}\text{Zr}_2\text{Si}_x\text{P}_{3-x}\text{O}_{12}$ ) because of its high ionic conductivity, wide window of electrochemical stability and stability in air. Hong [20] and Goodenough [21] were the first to study  $\text{Na}_{1+x}\text{Zr}_2\text{Si}_x\text{P}_{3-x}\text{O}_{12}$ . The highest ionic conductivity was  $10^{-4} \text{ S cm}^{-1}$  ( $x = 2$ ) at room temperature [20,22]. It has also been further improved by doping modifications

of NASICON. The rare earth element La-doped  $\text{Na}_3\text{Zr}_2\text{Si}_2\text{PO}_{12}$  has an ionic conductivity comparable with that of ionic liquid electrolytes ( $10^{-1} \text{ S cm}^{-1}$ ) [23].

In recent years, several studies have reported anion-assisted ways to increase the room temperature's ionic conductivity [23–25]. Lu et al. modified the  $\text{Li}_{6.25}\text{Ga}_{0.25}\text{La}_3\text{Zr}_2\text{O}_{12}$  crystals via  $\text{F}^-$ -assisted synthesis to generate smoother and quicker diffusion channels for  $\text{Li}^+$ , thus improving the ionic conductivity [23]. Li et al. reported that anion-substituted  $\text{Li}_{3x}\text{La}_{2/3-x}\text{TiO}_3$  has a higher ionic conductivity [24]. Goodenough reports that the substitution of F for OH, which allows  $\text{Li}_2(\text{OH})_{0.9}\text{F}_{0.1}\text{Cl}$  to have an improved  $\text{Li}^+$  diffusion path [26]. Although anion-assisted NZSPs have high ionic conductivity, they still do not provide effective inhibition of dendrite growth, resulting in uneven Na plating or streaking, leading to poor cell performance. This is because voids still exist on the surface of the SSE, leading to the uneven deposition of Na on the electrode surface and promoting the growth of dendrites. Here, we investigated  $\text{F}^-$ -assisted NZSP solid electrolyte materials. It was found that the grain size and densities of NZSP increased with the introduction of F. However, it is still not enough to inhibit the growth of Na dendrites. Then, we prepared a composite system by depositing epoxy into the pores of NZSPF via vacuum adsorption. The composite system greatly modified the cycling performance of the cell with almost no decrease in ionic conductivity and no increase in impedance. The ionic conductivity of epoxy-NZSPF<sub>0.7</sub> is  $0.67 \text{ mS cm}^{-1}$  (NZSPF<sub>0.7</sub> is  $0.95 \text{ mS cm}^{-1}$ ). In addition, epoxy-NZSPF<sub>0.7</sub> has a wider electrochemical stability window. Finally, we also assembled a  $\text{Na} \mid \text{epoxy-NZSPF}_{0.7} \mid \text{Na}_3\text{V}_2(\text{PO}_4)_3$  quasi-solid SIB, with good cycling performance at  $40^\circ\text{C}$ .

## 2. Materials and Methods

### 2.1. Synthesis of NZSPF<sub>x</sub> Solid Electrolyte

Traditional solid-phase reactions were adopted to synthesize  $\text{F}^-$ -assisted NZSPF<sub>x</sub> materials.  $\text{Na}_2\text{CO}_3$ ,  $\text{ZrO}_2$ ,  $\text{SiO}_2$ , and  $\text{NH}_4\text{H}_2\text{PO}_4$  were weighed according to certain stoichiometric ratios and then  $x$  mol of NaF ( $x = 0, 0.1, 0.3, 0.5, 0.7$ , and  $1.0$ ) was added separately. The final results were labeled NZSPF<sub>x</sub>. Balls, materials and ethanol were added to the ball mill tank in the ratio of 32:5:8. The milling was then carried out with a planetary ball mill at 400 rpm for 10 h. The 12 h drying of precursors was carried out under vacuum at  $80^\circ\text{C}$ ; then, the mixtures were transferred to a muffle furnace for 12 h preheating at  $900^\circ\text{C}$ , followed by 3 h sintering at  $1050^\circ\text{C}$ . The sintered powders were further ball-milled at 200 rpm for 10 h to obtain a uniform powder size. During the ball-milling process, a 5% mass fraction of PVA solution was added to act as a binder. The pressing of powers into pellets (diameter 16 mm, thickness 1 mm) was carried out at 120 MPa. Finally, the 4 h sintering of pellets was carried out at  $800^\circ\text{C}$  to remove the PVA solution. After cooling to room temperature, the 24 h sintering of pellets was performed at  $1100^\circ\text{C}$  to obtain NZSPF<sub>x</sub> solid electrolyte.

### 2.2. Synthesis of Epoxy-NZSPF<sub>0.7</sub> Solid Electrolyte

The DGEBA (diglycidyl ether of bisphenol-A) and PACM (4,4'-diaminodicyclohexylmethane) were dissolved in THF in stoichiometric ratios to obtain  $1 \text{ mol L}^{-1}$  solutions, respectively. Then, the two solutions were mixed in a volume ratio of 2:1 (DGEBA:PACM) and stirred for 1 h. The sintered NZSPF ceramic sheets in 2.1 were completely immersed in the mixed solution, kept in a vacuum environment for 20 min and cycled three times. The sintering of pellets was carried out at  $150^\circ\text{C}$  for 24 h to obtain an epoxy-NZSPF<sub>x</sub> solid electrolyte.

### 2.3. Characterization and Measurements

A Bruker D8 Advance X-ray diffractometer configured with Cu K $\alpha$  radiation in the  $2\theta$  scope of  $10\text{--}60^\circ$  was adopted to collect the X-ray diffraction (XRD) patterns, and the collection of data was carried out at  $5^\circ \text{ min}^{-1}$ . The chemical component in an Escalab 250Xi instrument from Thermo Scientific configured with an Al K $\alpha$  micro-focused X-ray

source was demonstrated via X-ray photoelectron spectroscopy (XPS) tests. The collection of Fourier transform infrared (FTIR) spectra were carried out on a Nicoletis 10 spectrometer from Thermo Scientific. The spectrum was from  $4000\text{ cm}^{-1}$  to  $400\text{ cm}^{-1}$ . The microstructures of SSE were studied using scanning electron microscopy (SEM) (QUNATA-FEG). The measurement of thermostability was carried out via thermogravimetric analysis (TGA) on a Netzch STA449F3 analyzer under  $\text{N}_2$  conditions at a heating rate of  $10\text{ }^{\circ}\text{C}/\text{min}$  from 25 to  $700\text{ }^{\circ}\text{C}$ .

A CHI660E (ChenHua) electrochemical workstation with an AC amplitude of  $10\text{ mV}$  and a frequency scope from  $10\text{ Hz}$  to  $10^6\text{ Hz}$  was adopted to make electrochemical impedance spectroscopy (EIS) tests at room temperature. A combination of direct-current (DC) polarization and alternating-current (AC) impedance was used for the ion transference number test. A CR2032 cell case was chosen to assemble a  $\text{Na}/\text{NZSPF}_x/\text{Na}$  symmetric battery. An AC impedance test is performed on the battery before the DC polarization test; then, a small bias voltage ( $5\text{ mV}$ ) is added to the battery for the DC polarization test, and after the planned current of the battery is stabilized, the battery is then tested for AC impedance again. The electrochemical stability windows of  $\text{NZSPF}_{0.7}$  and epoxy- $\text{NZSPF}_{0.7}$  solid electrolytes were evaluated with cyclic voltammetry (CV) and linear sweep voltammetry (LSV). The tests were performed on the  $\text{Au}/\text{NZSPF}_{0.7}/\text{Na}$  and  $\text{Au}/\text{epoxy-NZSPF}_{0.7}/\text{Na}$  cells and the scanning rate was  $0.2\text{ mV s}^{-1}$  at room temperature. The electrochemical stability test was carried out to test the interfacial stability and Na stripping–plating behavior. The testing of assembled  $\text{Na}/\text{NZSPF}_x/\text{Na}$  and  $\text{Na}/\text{epoxy-NZSPF}_{0.7}/\text{Na}$  symmetric cells was carried out on a Blue Power Test System CT2001A with a constant current density of  $0.1\text{ mA cm}^{-2}$  at  $40\text{ }^{\circ}\text{C}$ .

The assembly of the full cell was carried out in an argon atmosphere glove box using Na metal as the anode,  $\text{NZSPF}_{0.7}$  and epoxy- $\text{NZSPF}_{0.7}$  as the solid electrolyte, and  $\text{Na}_3\text{V}_2(\text{PO}_4)_3$  as the cathode using a 2032 cell case. For the preparation of the cathode electrode sheet,  $\text{Na}_3\text{V}_2(\text{PO}_4)_3$ , the mixture of acetylene black carbon and PVDF was carried out in NMP with a mass ratio of 7:2:1. Using Al foil as a fluid collector, the coating of the slurry was carried out on the surface of Al foil, followed by 12 h OF drying under vacuum at  $80\text{ }^{\circ}\text{C}$  to eliminate the NMP solvent. The Na metal, solid electrolyte and cathode pole piece were assembled in the order of  $\text{Na}/\text{epoxy-NZSPF}_{0.7}/\text{Na}_3\text{V}_2(\text{PO}_4)_3$ . The addition of  $10\text{ }\mu\text{L}$  liquid electrolyte (ethylene carbonate (EC) as the solvent and  $\text{NaClO}_4$  as the salt) was conducted between the solid electrolyte and the pole pieces to wet the contact surface. The constant current charge/discharge test of the batteries was performed on the LAND CT2001A test system at  $40\text{ }^{\circ}\text{C}$  to evaluate the long-cycle performance.

### 3. Results and Discussion

To investigate the influence of adding  $\text{F}^-$ , we used XRD to measure the lattice structure of samples with different fluorine contents. According to Figure S1, the main diffraction peaks of  $\text{NZSPF}_x$  ( $x = 0, 0.1, 0.3, 0.5, 0.7$ , and  $1.0$ ) are consistent with the monoclinic NZSP structure [27]. This phenomenon proves that the introduction of  $\text{F}^-$  did not destroy the crystal structure. However, with the increase in  $\text{NaF}$  content, a  $\text{ZrO}_2$  secondary phase was detected. This may be due to the reaction of  $\text{Si}^{4+}/\text{P}^{5+}$  with F during the process of high-temperature sintering, as it leads to a reduction in  $\text{Si}^{4+}/\text{P}^{5+}$  content and, finally, the deposition of the  $\text{ZrO}_2$  secondary phase. In addition, no fluorine-related phases were observed in the XRD patterns of all samples, which could be due to F occupying positions in the lattice dot matrix or high-temperature volatilization.

These featured peaks of P-O and Si-O groups (Figure S2) were analyzed with FTIR spectroscopy. All samples displayed the same stretching or bending vibration pattern. The peaks at  $598$  and  $1128\text{ cm}^{-1}$  were ascribed to P-O stretching in tetrahedral  $\text{PO}_4^{3-}$  units [25,27], while the peaks at  $501$  and  $863\text{ cm}^{-1}$  were ascribed to the Si-O stretching in tetrahedral  $\text{SiO}_4^{4-}$  units [25,28]. These outcomes definitively prove that  $\text{SiO}_4^{4-}$  and  $\text{PO}_4^{3-}$  units are in the  $\text{NZSPF}_x$  crystal structure. These peaks are shifted to varying degrees,

presumably due to F occupying the position of the O element in the  $\text{NZSPF}_x$  lattice, causing the conformity of positive and negative centers in the lattice [26].

To further investigate the elemental composition of  $\text{NZSPF}_x$ , XPS was used to characterize NZSP,  $\text{NZSPF}_{0.7}$ . Figure S3a shows the full XPS spectra of NZSP and  $\text{NZSPF}_{0.7}$ . Different peak areas corresponding to Na, Zr, Si, P, O are obviously found, which proves that the major components of the ceramics is  $\text{NZSPF}_{0.7}$ . High-resolution XPS (Figure S3b) is adopted to detect the F 1s peak, which proves the successful doping of the F element. The binding energy at 684 eV corresponds to the F-Si/P bond [29,30], showing that the  $\text{F}^-$  takes up the  $\text{O}^{2-}$  place in the  $\text{NZSPF}_x$  lattice. The intensities of the P 2p and Si 2p peaks reduce slightly under the help of  $\text{F}^-$  (Figure S3c,d), indicating a slight decrease in the concentration of  $\text{P}^{5+}$  and  $\text{Si}^{4+}$  because of the reaction of  $\text{P}^{5+}/\text{Si}^{4+}$  with F and the volatilization of the results at high temperatures. In addition, a slight shift in P 2p and Si 2p to a higher binding energy was observed in  $\text{NZSPF}_{0.7}$  by comparing with the undoped sample, and the presence of P/Si-F bonds [31] can explain this shift, which also proves that  $\text{F}^-$  takes up part of the  $\text{O}^{2-}$  sites in the  $\text{NZSPF}_{0.7}$  lattice.

Although the doping of NaF can reduce the resistance of NZSP (Figure S5) and improve the ionic conductivity (Figure S6), the cycling stability is deemed unsatisfactory (Figure S7). This is because the  $\text{NZSPF}_{0.7}$  grain boundaries are not dense, which also leads to the ability of growing and forming Na dendrites in the crevices (Figure S9). Therefore, it is necessary to modify  $\text{NZSPF}_{0.7}$  to strengthen the interface between the SSE and the electrode, and to stop the development of Na dendrites.

Figure 1a shows the FTIR spectra of the epoxy,  $\text{NZSPF}_{0.7}$ , and epoxy- $\text{NZSPF}_{0.7}$  composite system. The FTIR spectra of epoxy- $\text{NZSPF}_{0.7}$  do not show new peaks, only a simple superposition of the two monomers. This indicates that no new substances are produced in the composite system and no reaction occurs between the two monomers. Figure 1b shows the TGA curves of epoxy,  $\text{NZSPF}_{0.7}$ , and epoxy- $\text{NZSPF}_{0.7}$ . It can be seen that in the tested temperature range,  $\text{NZSPF}_{0.7}$  does not undergo mass loss and is thermally stable, while the mass loss of epoxy starts to occur at 300 °C and almost completely decomposes after reaching 600 °C. This coincides with the weight loss range of the composite system, and it can be determined that the mass loss of the composite system is caused by epoxy. This indicates that epoxy was successfully filled into the voids of  $\text{NZSPF}_{0.7}$ , further improving the densities of the ceramics (Figure S10).

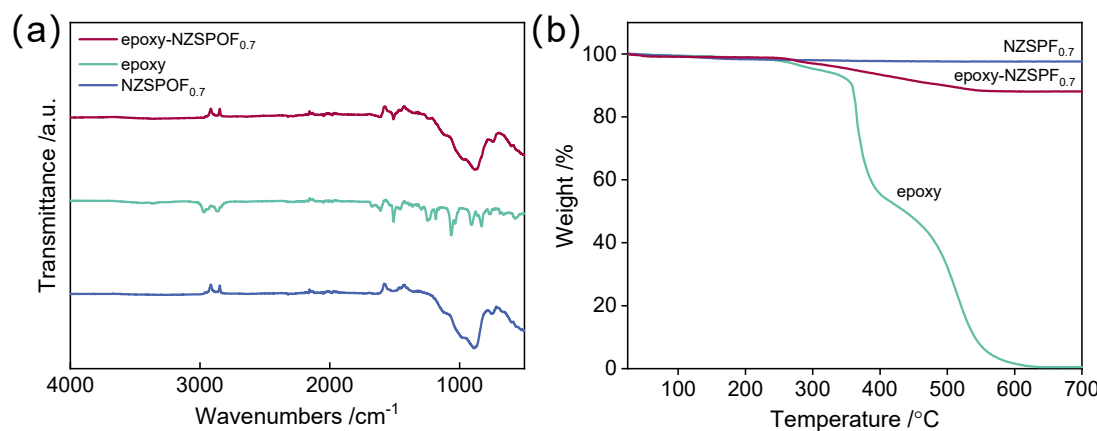


**Figure 1.** (a) FTIR spectra and (b) TGA analysis for  $\text{NZSPF}_{0.7}$ , epoxy and epoxy- $\text{NZSPF}_{0.7}$ .

To observe the surface difference between  $\text{NZSPF}_{0.7}$  and epoxy- $\text{NZSPF}_{0.7}$ , and the distribution of epoxy resin in  $\text{NZSPF}_{0.7}$ , SEM and EDS tests were performed on both  $\text{NZSPF}_{0.7}$  (Figure S4) and epoxy- $\text{NZSPF}_{0.7}$  (Figure 2). Figure S4 shows the SEM image of  $\text{NZSPF}_{0.7}$ . The SEM images show that with the growth in NaF content, the size of  $\text{NZSPF}_x$  grains gradually grows larger. However, F promotes grain growth, reduces grain boundary concentration and increases ceramic density to a certain extent, which can efficiently decrease the grain boundary concentration, increase the ionic conductivity and reduce

the grain boundary resistance [32,33]. There are still a large number of interstices in the middle of the ceramic after high-temperature sintering, and the existence of these interstices leads to uneven deposition of dendrites here and reduces the electrochemical performance. Figure 2 shows the surface of epoxy-NZSPF<sub>0.7</sub> composite solid electrolyte after polishing; compared with NZSPF<sub>0.7</sub>, the gap in the composite system is significantly reduced, which is a good verification of the increased densities. The denseness of epoxy-NZSPF<sub>0.7</sub> is 97.6% and NZSPF<sub>0.7</sub> is 93.4%, while that of un-assisted NZSP is only 79.8%. This shows that the filling of epoxy can raise the densities of the composite system because the prior condition for a solid electrolyte to have a high ionic conductivity is a high density [34,35]. Additionally, Figure 2c displays the EDS discussion on the epoxy-NZSPF<sub>0.7</sub> ceramic sample. Because epoxy contains a large number of C elements, by observing the distribution of C elements, we can find that epoxy is evenly distributed in the composite system. The maps also confirm that O, P, Si, F, Na and Zr factors generally show an even homogeneous distribution in the composite system, and the content of the F element is essentially the same as that of NASPF<sub>0.7</sub>.

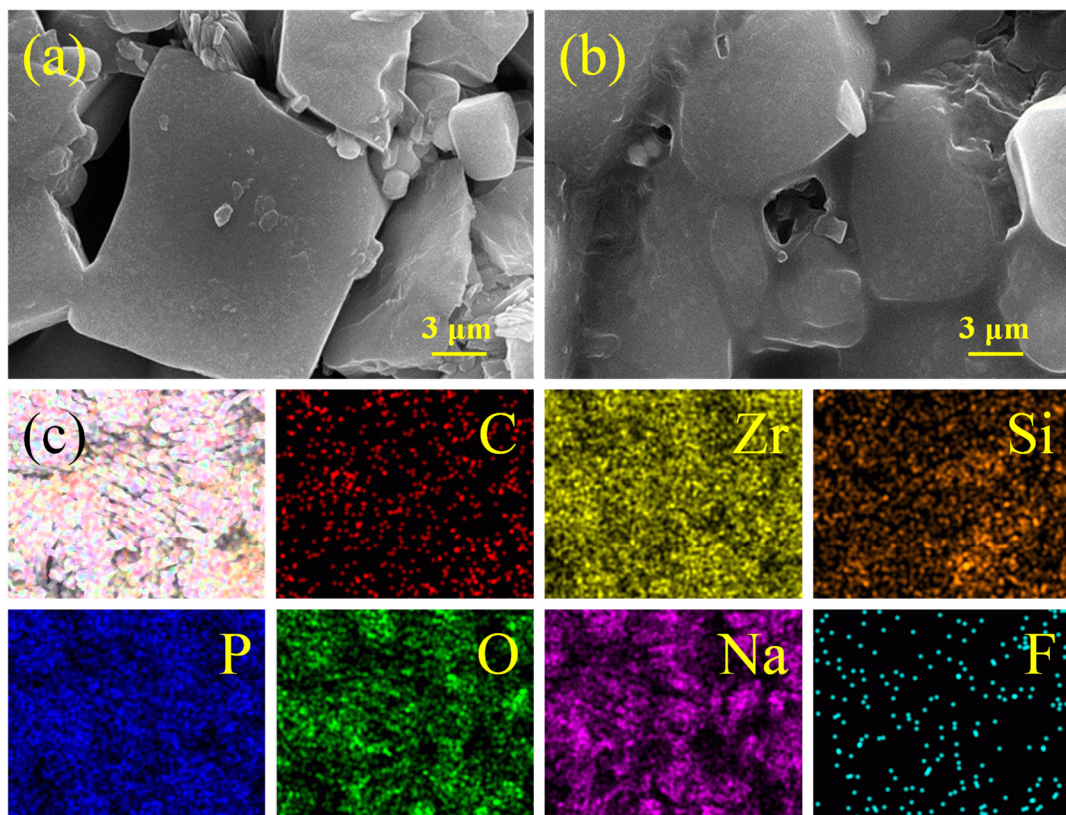


**Figure 2.** SEM image of (a) NZSPF<sub>0.7</sub> and (b) epoxy-NZSPF<sub>0.7</sub>; (c) EDS mapping of epoxy-NZSPF<sub>0.7</sub>.

The electrical conductivities of the solid electrolyte were investigated with EIS. Figure 3a displays the impedance spectra of NZSPF<sub>0.7</sub> and epoxy-NZSPF<sub>0.7</sub>. According to the Nyquist curve, the resistance of NZSPF<sub>0.7</sub> and epoxy-NZSPF<sub>0.7</sub> are calculated as 370 Ω and 420 Ω. The overall conductivity measures from the EIS are 0.95 and 0.67 mS cm<sup>-1</sup>. The impedance of epoxy-NZSPF<sub>0.7</sub> becomes larger and the ionic conductivity decreases are due to the fact that the epoxy impedance of the pure phase is extremely large; therefore, filling the gap to NZSPF<sub>0.7</sub> results in a growth in the impedance and a decline in the ionic conductivity of epoxy-NZSPF<sub>0.7</sub>.

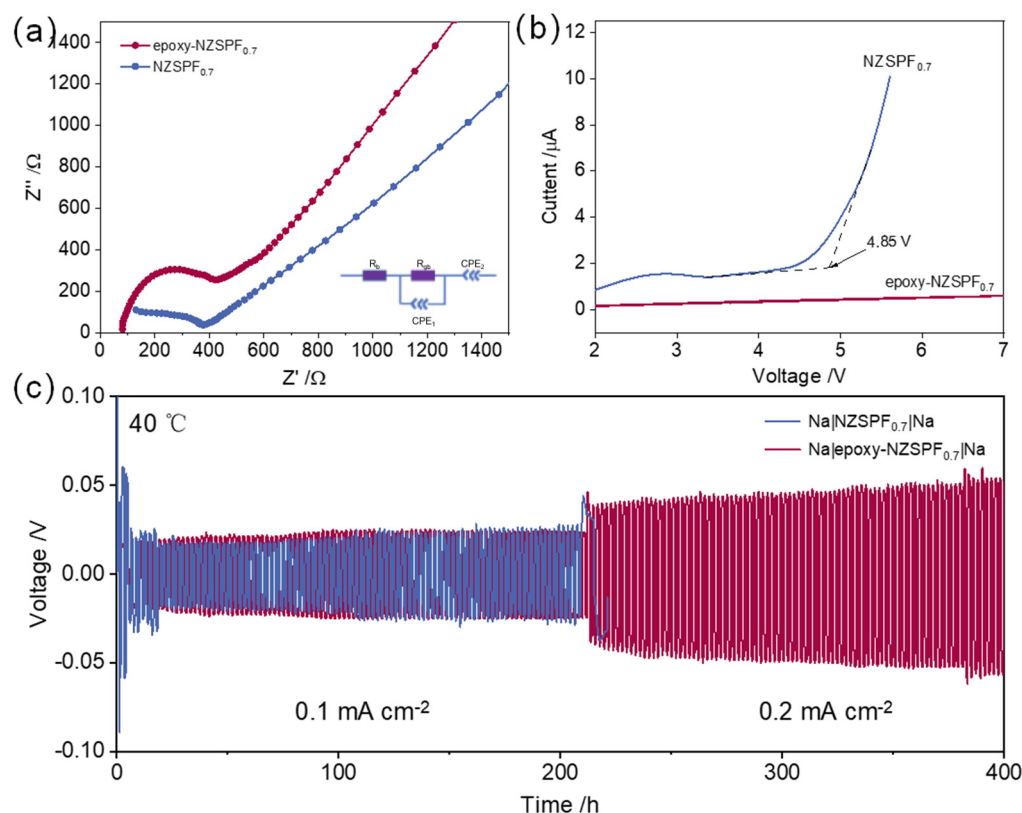


**Figure 3.** (a) EIS measurements at room temperature; (b) LSV of the  $\text{Au}|\text{NZSPF}_{0.7}|\text{Na}$  and  $\text{Au}|\text{epoxy}-\text{NZSPF}_{0.7}|\text{Na}$  cells at room temperature; (c) variable current cycling of  $\text{Na}|\text{NZSPF}_{0.7}|\text{Na}$  and  $\text{Na}|\text{epoxy}-\text{NZSPF}_{0.7}|\text{Na}$  symmetric cells (the current density is  $0.1 \text{ mA cm}^{-2}$  and becomes  $0.2 \text{ mA cm}^{-2}$  after 200 h).

To verify the conduction behavior of sodium ions, the sodium ion transfer number ( $t_{\text{Na}^+}$ ) was determined. The  $t_{\text{Na}^+}$  ( $40^\circ\text{C}$ ) of NZSPF<sub>0.7</sub> was 0.84, while that of epoxy-NZSPF<sub>0.7</sub> was 0.79. This proves that the filling of epoxy does not significantly affect the  $t_{\text{Na}^+}$  and  $\text{Na}^+$  is still transported by NZSPF<sub>0.7</sub> as a transport channel rather than epoxy.

In addition to having a high ionic conductivity, a wide-range electrochemical stability window is also a basic necessity for SSE in actual use. The electrochemical stability windows of NZSPF<sub>0.7</sub> and epoxy-NZSPF<sub>0.7</sub> is assessed via LSV with  $\text{Au}|\text{NZSPF}_{0.7}|\text{Na}$  and  $\text{Au}|\text{epoxy}-\text{NZSPF}_{0.7}|\text{Na}$  batteries with a scan rate of  $0.2 \text{ mV s}^{-1}$  at  $30^\circ\text{C}$  (Figure 3b). The electrochemical stability window of the NZSPF<sub>0.7</sub> is 4.85 V, while the current intensity of epoxy-NZSPF<sub>0.7</sub> remains constant in the range of 2–7 V. This indicates that the electrochemical steadiness window of the epoxy-NZSPF<sub>0.7</sub> up to 7 V. It is expected that epoxy-NZSPF<sub>0.7</sub> can be used as a high-voltage sodium battery. The electrochemical properties of NZSPF<sub>0.7</sub>, NZSPF<sub>0.7</sub> and epoxy-NZSPF<sub>0.7</sub> are listed in Table 1.

**Table 1.** Electrochemical properties of NZSPF<sub>0</sub>, NZSPF<sub>0.7</sub> and epoxy-NZSPF<sub>0.7</sub>.

Sample	Impedance at Room Temperature	Ionic Conductivity	Ion Transfer Number	Electrochemical Stabilization Window
NZSPF <sub>0</sub>	1527	0.45	0.68	-
NZSPF <sub>0.7</sub>	370 $\Omega$	$0.95 \text{ mS cm}^{-1}$	0.84	4.85 V
epoxy-NZSPF <sub>0.7</sub>	420 $\Omega$	$0.67 \text{ mS cm}^{-1}$	0.79	7 V

Figure 3c shows that epoxy-NZSPF<sub>0.7</sub> can be cycled steadily for above 200 h (100 cycles) at a current density of  $0.1 \text{ mA cm}^{-2}$  with no fluctuation in potential, and remains stable for nearly 200 h when the current density grows to  $0.2 \text{ mA cm}^{-2}$ . This indicates that

epoxy-NZSPF<sub>0.7</sub> can promote the even deposition of Na<sup>+</sup> and stop the Na dendrites from developing. In contrast, NZSPF<sub>0.7</sub> could only keep steady at 0.1 mA cm<sup>-2</sup> and immediately short-circuited at 0.2 mA cm<sup>-2</sup>. It can be noted that NZSPF<sub>0.7</sub> needs 5–10 h to adapt to the electrode with significant potential fluctuations, while epoxy-NZSPF<sub>0.7</sub> hardly needs this process. Compared to this, epoxy-NZSPF<sub>0.7</sub> requires a shorter activation time and does not show significant short-circuiting after increasing the current, indicating that it has higher electrode stability.

Finally, Na|NZSPF<sub>0.7</sub>|Na<sub>3</sub>V<sub>2</sub>(PO<sub>4</sub>)<sub>3</sub> and Na|epoxy-NZSPF<sub>0.7</sub>|Na<sub>3</sub>V<sub>2</sub>(PO<sub>4</sub>)<sub>3</sub> solid SIBs were assembled. Figure 4 shows the performances of batteries. The polarization of NZSPF<sub>0.7</sub> is bigger with the gradual current rate growth (Figure 4a), while the charge/discharge curve of epoxy-NZSPF<sub>0.7</sub> is smooth and the polarization is basically unchanged (Figure 4b). The discharge specific capacities of epoxy-NZSPF<sub>0.7</sub> are 96.9, 80.1, 68.9 and 48.9 mAh g<sup>-1</sup> at 0.1C, 0.5C, 1C and 2C. In the case of the reversion of the current density to 1C and 0.5C, the given capacities are 60.8 and 70.5 mAh g<sup>-1</sup> (Figure 4c). This shows that when the current returns to the same rates, it has excellent reversibility and steadiness, although the reversible capacity is slightly reduced. Figure 4d shows the cycling performance of cells assembled with two different electrolytes at a current density of 0.1C at 40 °C. The discharge-specific capacity remains 93.7 mAh g<sup>-1</sup> after 150 cycles, which is 95.8% capacity retention of initial capacity (97.8 mAh g<sup>-1</sup>). The mean coulombic efficiency is close to 99%, which is only 79.1% for Na<sub>3</sub>V<sub>2</sub>(PO<sub>4</sub>)<sub>3</sub>|NZSPF<sub>0.7</sub>|Na battery.

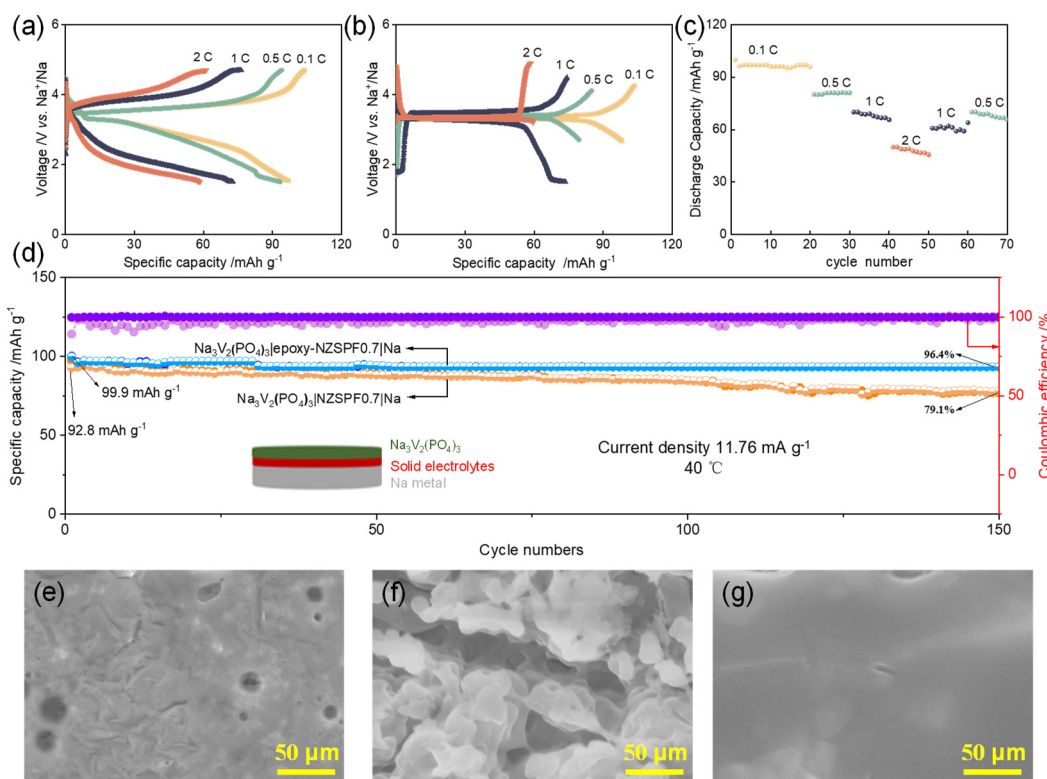


**Figure 4.** (a) Charging–discharging profiles of Na<sub>3</sub>V<sub>2</sub>(PO<sub>4</sub>)<sub>3</sub> | NZSPF<sub>0.7</sub> | Na at different rates; (b,c) charging–discharging profiles of Na<sub>3</sub>V<sub>2</sub>(PO<sub>4</sub>)<sub>3</sub> | epoxy–NZSPF<sub>0.7</sub> | Na at different rates; (d) cycling performance of the Na<sub>3</sub>V<sub>2</sub>(PO<sub>4</sub>)<sub>3</sub> | epoxy–NZSPF<sub>0.7</sub> | Na battery at a current density of 11.76 mA g<sup>-1</sup>; (e) SEM image of sodium metal surface before cycling; SEM image of sodium metal surface of (f) Na<sub>3</sub>V<sub>2</sub>(PO<sub>4</sub>)<sub>3</sub> | NZSPF<sub>0.7</sub> | Na battery and (g) Na<sub>3</sub>V<sub>2</sub>(PO<sub>4</sub>)<sub>3</sub> | epoxy–NZSPF<sub>0.7</sub> | Na battery after 150 cycles.

Figure 4e–g shows the SEM images of the Na electrode surface. Obviously, after 150 cycles, Na dendrites were formed at the boundaries and voids of the NZSPF<sub>0.7</sub> solid electrolyte (Figure 4f), resulting in inhomogeneous Na plating/stripping with a corre-

sponding aggravation of the cell behavior [30]. However, the Na electrode surface of  $\text{Na}_3\text{V}_2(\text{PO}_4)_3 \mid \text{epoxy-NZSPF}_{0.7} \mid \text{Na}$  battery was clean and smooth (Figure 4g), and almost no Na deposition was found, indicating that the epoxy-filled dielectric material can effectively prevent the formation of dendrites and enhance the battery cycling behavior.

#### 4. Conclusions and Outlook

In conclusion, the grain boundary concentration of NZSP was effectively reduced by introducing NaF into the NZSP solid electrolyte and a denser  $\text{NZSPF}_{0.7}$  with improved ionic conductivity was obtained ( $0.98 \text{ mS cm}^{-1}$ ); however,  $\text{NZSPF}_{0.7}$  did not stop the development of sodium dendrites well and had poor interfacial properties. For this reason, a composite solid electrolyte epoxy- $\text{NZSPF}_{0.7}$  was prepared via simply vacuum adsorption and by filling the interstitial space of  $\text{NZSPF}_{0.7}$  with epoxy and curing it. Epoxy- $\text{NZSPF}_{0.7}$  combines the great ionic conductivity of inorganic electrolytes as well as the good interfacial contact from organic polymer electrolytes, with high ionic conductivity ( $0.67 \text{ mS cm}^{-1}$ ) as well as excellent interfacial performance and cycling behavior (the initial capacity of cells is  $97.9 \text{ mAh g}^{-1}$  with a 96.4% retention rate after 150 turns). According to the above-presented results, this study may offer a novel idea for research concerning solid electrolytes for sodium-ion batteries.

**Supplementary Materials:** The following supporting information can be downloaded at: <https://www.mdpi.com/article/10.3390/batteries9060331/s1>. Figure S1. (a) XRD patterns of  $\text{NZSPFx}$  ( $x = 0, 0.1, 0.3, 0.5, 0.7$ , and  $1.0$ ); Figure S2. FTIR spectra of  $\text{NZSPFx}$  ( $x = 0, 0.1, 0.3, 0.5, 0.7$ , and  $1.0$ ); Figure S3. XPS spectra of (a) survey spectra, (b) F 1s, (c) P 2p and (d) Si 2p of  $\text{NZSPF}_{0.7}$ ; Figure S4. SEM images of  $\text{NZSPFx}$  ceramic pellets, (a)  $x = 0$ , (b)  $x = 0.1$ , (c)  $x = 0.3$ , (d)  $x = 0.5$ , (e)  $x = 0.7$ , and (f)  $x = 1.0$ ; (g,h) the corresponding elemental mapping in the square of (e) image; (h) densities and relative densities of  $\text{NZSPFx}$ ; Figure S5. EIS measurements performed of  $\text{NZSPFx}$  ( $x = 0, 0.1, 0.3, 0.5, 0.7$ , and  $1.0$ ) solid electrolytes; Figure S6. Ion conductivity (red) and ion transfer number (blue) of  $\text{NZSPFx}$  ( $x = 0, 0.1, 0.3, 0.5, 0.7$ , and  $1.0$ ) solid electrolytes; Figure S7. cycling performance of  $\text{Na}_3\text{V}_2(\text{PO}_4)_3 \mid \text{NZSPF}_{0.7} \mid \text{Na}$  battery; Figure S8. Arrhenius plots of  $\text{NZSPFx}$  ( $x = 0, 0.1, 0.3, 0.5, 0.7$ , and  $1.0$ ) solid electrolytes; Figure S9. SEM images of the sodium metal surface of cell  $\text{Na}_3\text{V}_2(\text{PO}_4)_3 \mid \text{NZSPF}_{0.7} \mid \text{Na}$  (a) before and (b) after cycling; Figure S10. The densities of  $\text{NZSPF}_{0.7}$  and epoxy- $\text{NZSPF}_{0.7}$ ; Figure S11. Variable current cycling of  $\text{Na} \mid \text{NZSPF}_{0.7} \mid \text{Na}$  symmetric cells (the current density is  $0.1 \text{ mA cm}^{-2}$  and becomes  $0.2 \text{ mA cm}^{-2}$  after 200 h); Figure S12. Variable current cycling of  $\text{Na} \mid \text{epoxy-NZSPF}_{0.7} \mid \text{Na}$  symmetric cells (the current density is  $0.1 \text{ mA cm}^{-2}$  and becomes  $0.2 \text{ mA cm}^{-2}$  after 200 h); Table S1. Chemical composition for  $\text{NZSPFx}$  ( $x = 0, 0.1, 0.3, 0.5, 0.7, 1.0$ ).

**Author Contributions:** Y.F.: conceptualization, data analysis, and writing of the original draft. D.L.: experimental execution, data analysis and discussion. Y.S.: experimental execution and discussion. G.Z.: writing-review and editing. H.G.: research design, funding supporting and supervision. All authors have read and agreed to the published version of the manuscript.

**Funding:** The authors acknowledge financial support provided the Key National Natural Science Foundation of Yunnan Province (2019FY003023).

**Institutional Review Board Statement:** Not applicable, as studies on humans and animals are not involved.

**Informed Consent Statement:** Not applicable, as studies on humans are not involved.

**Data Availability Statement:** The data are not publicly available due to the data required to reproduce these findings forming part of an ongoing study.

**Acknowledgments:** The authors acknowledge financial support provided by the National Natural Science Foundation of China (No. 52064049), the National Natural Science Foundation of Yunnan Province (202301AS070040), Key Laboratory of Solid-State Ions for Green Energy of Yunnan University, the Electron Microscope Center of Yunnan University for the support of this work.

**Conflicts of Interest:** The authors declare no conflict of interest.

## References

- Chu, S.; Majumdar, A. Opportunities and challenges for a sustainable energy future. *Nature* **2012**, *7411*, 294–303. [[CrossRef](#)]
- Xu, K. Electrolytes and interphases in Li-ion batteries and beyond. *Chem. Rev.* **2014**, *23*, 11503–11618. [[CrossRef](#)]
- Yoo, H.D.; Liang, Y.L.; Li, Y.F.; Yao, Y. High areal capacity hybrid magnesium-lithium-ion battery with 99.9% coulombic efficiency for large-scale energy storage. *ACS Appl. Mater. Interfaces* **2015**, *12*, 7001–7007. [[CrossRef](#)]
- Hao, F.; Liang, Y.L.; Zhang, Y.; Chen, Z.Y.; Zhang, J.B.; Ai, Q.; Guo, H.; Fan, Z.; Lou, J.; Yao, Y. High-energy all-solid-state organic-lithium batteries based on ceramic electrolytes. *ACS Energy Lett.* **2021**, *1*, 201–207. [[CrossRef](#)]
- Yabuuchi, N.; Kubota, K.; Dahbi, M.; Komaba, S. Research Development on sodium-ion batteries. *Chem. Rev.* **2014**, *23*, 11636–11682. [[CrossRef](#)] [[PubMed](#)]
- Che, H.Y.; Chen, S.L.; Xie, Y.Y.; Wang, H.; Amine, K.; Liao, X.Z.; Ma, Z.F. Electrolyte design strategies and research progress for room-temperature sodium-ion batteries. *Energy Environ. Sci.* **2017**, *5*, 1075–1101. [[CrossRef](#)]
- Cheng, X.B.; Zhang, R.; Zhao, C.Z.; Zhang, Q. Toward safe lithium metal anode in rechargeable batteries: A Review. *Chem. Rev.* **2017**, *15*, 10403–10473. [[CrossRef](#)]
- Cohn, A.P.; Muralidharan, N.; Carter, R.; Share, K.; Pint, C.L. Anode-free sodium battery through in situ Plating of sodium metal. *Nano Lett.* **2017**, *2*, 1296–1301. [[CrossRef](#)]
- Fu, K.; Gong, Y.H.; Hitz, G.T.; McOwen, D.W.; Li, Y.J.; Xu, S.M.; Wen, Y.; Zhang, L.; Wang, C.W.; Pastel, G.; et al. Three-dimensional bilayer garnet solid electrolyte based high energy density lithium metal-sulfur batteries. *Energy Environ. Sci.* **2017**, *7*, 1568–1575. [[CrossRef](#)]
- Li, H.S.; Ding, Y.; Ha, H.; Shi, Y.; Peng, L.L.; Zhang, X.G.; Ellison, C.J.; Yu, G.H. An all-stretchable-component sodium-ion full battery. *Adv. Mater.* **2017**, *29*, 1700898. [[CrossRef](#)]
- Zhao, Y.; Goncharova, L.V.; Lushington, A.; Sun, Q.; Yadegari, H.; Wang, B.Q.; Xiao, W.; Li, R.Y.; Sun, X.L. Superior stable and long life sodium metal anodes achieved by atomic layer dposition. *Adv. Mater.* **2017**, *29*, 1606663. [[CrossRef](#)]
- Liu, H.; Guo, H.; Liu, B.H.; Liang, M.F.; Lv, Z.L.; Adair, K.R.; Sun, X.L. Few-layer MoSe<sub>2</sub> nanosheets with expanded (002) planes confined in hollow carbon nanospheres for ultrahigh-performance Na-ion batteries. *Adv. Funct. Mater.* **2018**, *28*, 1707480. [[CrossRef](#)]
- Zhao, C.L.; Liu, L.L.; Qi, X.G.; Lu, Y.X.; Wu, F.X.; Zhao, J.M.; Yu, Y.; Hu, Y.S.; Chen, L.Q. Solid-state sodium batteries. *Adv. Energy Mater.* **2018**, *17*, 1601196. [[CrossRef](#)]
- Kwak, H.; Lyoo, J.; Park, J.; Han, Y.; Asakura, R.; Remhof, A.; Battaglia, C.; Kim, H.; Hong, S.T.; Jung, Y.S. Na<sub>2</sub>ZrC<sub>16</sub> enabling highly stable 3 V all-solid-state Na-ion batteries. *Energy Storage Mater.* **2021**, *37*, 47–54. [[CrossRef](#)]
- He, X.Z.; Ji, X.; Zhang, B.; Rodrigo, N.D.; Hou, S.; Gaskell, H.; Deng, T.; Wan, H.L.; Liu, S.F.; Xu, J.J.; et al. Tuning interface lithiophobicity for lithium metal solid-state batteries. *ACS Energy Lett.* **2022**, *7*, 131–139. [[CrossRef](#)]
- Bay, M.C.; Grissa, R.; Egorov, K.V.; Asakura, R.; Batrtaglia, C. Low Na-β''-alumina electrolyte/cathode interfacial resistance enabled by a hydroborate electrolyte opening up new cell architecture designs for all-solid-state sodium batteries. *Mater. Futures* **2022**, *1*, 031001. [[CrossRef](#)]
- Will, F.G. Effect of water on beta alumina conductivity. *J. Electrochem. Soc.* **1976**, *6*, 834–836. [[CrossRef](#)]
- Zhang, L.; Yang, K.; Mi, J.L.; Lu, L.; Zhao, L.R.; Wang, L.M.; Li, Y.M.; Zeng, H. Na<sub>3</sub>PSe<sub>4</sub>: A novel chalcogenide solid electrolyte with high Ionic conductivity. *Adv. Energy Mater.* **2015**, *5*, 1501294. [[CrossRef](#)]
- Chi, X.W.; Liang, Y.L.; Hao, F.; Zhang, Y.; Whiteley, J.; Dong, H.; Hu, P.; Lee, S.; Yao, Y. Tailored organic electrode material compatible with sulfide electrolyte for stable all-solid-state sodium batteries. *Angew. Chem. Int. Edit.* **2018**, *10*, 2630–2634. [[CrossRef](#)]
- Hong, H.Y.P. Crystal-structures and crystal-chemistry in system Na<sub>1+x</sub>Zr<sub>2</sub>SixP<sub>3-x</sub>O<sub>12</sub>. *Mater. Res. Bull.* **1976**, *2*, 173–182. [[CrossRef](#)]
- Goodenough, J.B.; Hong, H.Y.P.; Kafalas, J.A. Fast Na<sup>+</sup>-ion yransport in skeleton structures. *Mater. Res. Bull.* **1976**, *2*, 203–220. [[CrossRef](#)]
- Wang, H.; Zhao, G.F.; Wang, S.M.; Liu, D.L.; Mei, Z.Y.; An, Q.; Jiang, J.W.; Guo, H. Enhanced ionic conductivity of a Na<sub>3</sub>Zr<sub>2</sub>Si<sub>2</sub>PO<sub>12</sub> solid electrolyte with Na<sub>2</sub>SiO<sub>3</sub> obtained by liquid phase sintering for solid-state Na<sup>+</sup> batteries. *Nanoscale* **2022**, *14*, 823–832. [[CrossRef](#)] [[PubMed](#)]
- Lu, Y.; Meng, X.Y.; Alonso, J.A.; Fernandez-Diaz, M.T.; Sun, C.W. Effects of fluorine doping on structural and electrochemical properties of Li<sub>6.25</sub>Ga<sub>0.25</sub>La<sub>3</sub>Zr<sub>2</sub>O<sub>12</sub> as electrolytes for solid-state lithium batteries. *ACS Appl. Mater. Interfaces* **2019**, *2*, 2042–2049. [[CrossRef](#)]
- Li, J.X.; Wen, Z.Y.; Xu, X.X.; Zhu, X.J. Lithium-ion conduction in the anion substituted La<sub>2/3-x</sub>Li<sub>3x-y</sub>TiO<sub>3-y</sub>F<sub>y</sub> electrolyte with perovskite-type structure. *Solid State Ionics* **2005**, *29–30*, 2269–2273. [[CrossRef](#)]
- Li, Y.T.; Zhou, W.D.; Xin, S.; Li, S.; Zhu, J.L.; Lu, X.J.; Cui, Z.M.; Jia, Q.X.; Zhou, J.S.; Zhao, Y.S.; et al. Fluorine-doped antiperovskite electrolyte for all-solid-state lithium-ion batteries. *Angew. Chem. Int. Edit.* **2016**, *34*, 9965–9968. [[CrossRef](#)]
- He, S.N.; Xu, Y.L.; Chen, Y.J.; Ma, X.N. Enhanced ionic conductivity of an F<sup>-</sup>-assisted Na<sub>3</sub>Zr<sub>2</sub>Si<sub>2</sub>PO<sub>12</sub>solid electrolyte for solid-state sodium batteries. *J. Mater. Chem. A* **2020**, *25*, 12594–12602. [[CrossRef](#)]
- Liu, C.; Wen, Z.Y.; Rui, K. High ion conductivity in garnet-type F-doped Li<sub>7</sub>La<sub>3</sub>Zr<sub>2</sub>O<sub>12</sub>. *Int. J. Inorg. Mater.* **2015**, *9*, 995–1000.
- Song, S.F.; Duong, H.M.; Korsunsky, A.M.; Hu, N.; Lu, L. A Na<sup>+</sup> superionic conductor for room-temperature sodium batteries. *Sci. Rep.* **2016**, *6*, 32330. [[CrossRef](#)]

29. Lee, S.H. Surface properties of fluoroethylene carbonate-derived solid electrolyte interface on graphite negative electrode by narrow-range cycling in cell formation process. *Appl. Surf. Sci.* **2014**, *322*, 64–70. [[CrossRef](#)]
30. Kanezashi, M.; Matsutani, T.; Wakihara, T.; Nagasawa, H.; Okubo, T.; Tsuru, T. Preparation and has permeation properties of fluorine-silica membranes with controlled amorphous silica structures: Effect of fluorine source and calcination temperature on network size. *ACS Appl. Mater. Interfaces* **2017**, *29*, 24625–24633. [[CrossRef](#)]
31. Dalavi, S.; Guduru, P.; Lucht, B.L. Performance enhancing electrolyte additives for lithium ion batteries with silicon anodes. *J. Electrochem. Soc.* **2012**, *5*, A642–A646. [[CrossRef](#)]
32. Ihlefeld, J.F.; Gurniak, E.; Jones, B.H.; Wheeler, D.R.; Rodriguez, M.A.; McDaniel, A.H. Scaling effects in sodium zirconium silicate phosphate ( $\text{Na}_{1+x}\text{Zr}_2\text{Si}_x\text{P}_{3-x}\text{O}_{12}$ ) ion-conducting thin films. *J. Am. Ceram. Soc.* **2016**, *8*, 2729–2736. [[CrossRef](#)]
33. Wang, H.; Sun, Y.J.; Liu, Q.; Mei, Z.Y.; Yang, L.; Duan, L.Y.; Guo, H. An asymmetric bilayer polymer-ceramic solid electrolyte for high-performance sodium metal batteries. *J. Energy Chem.* **2022**, *74*, 18–25. [[CrossRef](#)]
34. Xu, X.X.; Wen, Z.Y.; Yang, X.L.; Chen, L.D. Dense nanostructured solid electrolyte with high Li-ion conductivity by spark plasma sintering technique. *Mater. Res. Bull.* **2008**, *8–9*, 2334–2341. [[CrossRef](#)]
35. Fuentes, R.O.; Figueiredo, F.M.; Marques, F.M.B.; Franco, J.I. Influence of microstructure on the electrical properties of NASICON materials. *Solid State Ionics* **2001**, *1–2*, 173–179. [[CrossRef](#)]

**Disclaimer/Publisher's Note:** The statements, opinions and data contained in all publications are solely those of the individual author(s) and contributor(s) and not of MDPI and/or the editor(s). MDPI and/or the editor(s) disclaim responsibility for any injury to people or property resulting from any ideas, methods, instructions or products referred to in the content.